

**Quantitative in-vivo characterization of intracellular and  
extracellular pH profiles in heterogeneous tumors:  
a novel method enabling multiparametric pH analysis**

Norbert W. Lutz,<sup>1,\*</sup> Yann Le Fur,<sup>1</sup> Johanna Chiche,<sup>2</sup> Jacques  
Pouysségur,<sup>2,3</sup> Patrick J. Cozzone<sup>1</sup>

<sup>1</sup> Centre de Résonance Magnétique Biologique et Médicale, UMR 7339, Faculté de  
Médecine de la Timone, CNRS, Aix-Marseille Université, F-13005 Marseille, France

<sup>2</sup> Institute of Research on Cancer and Aging, UMR 7284, Centre Antoine Lacassagne,  
Université de Nice, F-06189 Nice, France

<sup>3</sup> Centre Scientifique de Monaco, MC-98000 Monaco-Ville, Monaco

*(J.C., present address: Contrôle Métabolique des Morts Cellulaires, INSERM U 1065,  
Centre Méditerranéen de Médecine Moléculaire, F-06204 Nice, France)*

\* Correspondence:

Norbert.Lutz@univ-amu.fr

phone: +33 491 324814

fax: +33 491 256539

**Running title:** Multiparametric study of tumor pH heterogeneity

**The authors disclose no potential conflicts of interest.**

## ABSTRACT

Acid production and transport are currently being studied to identify new targets for efficient cancer treatment, as subpopulations of tumor cells frequently escape conventional therapy owing to their particularly acidic tumor microenvironment. Heterogeneity in intracellular and extracellular tumor pH ( $\text{pH}_i$ ,  $\text{pH}_e$ ) has been reported, but none of the methods currently available for measuring tissue pH provides quantitative parameters characterizing pH distribution profiles in tissues. To this intent, we present here a multiparametric, noninvasive approach based on *in vivo*  $^{31}\text{P}$  NMR spectroscopy, and its application to mouse tumor xenografts. First, localized  $^{31}\text{P}$  NMR spectrum signals of  $\text{pH}_i$  and  $\text{pH}_e$  reporter molecules (inorganic phosphate,  $\text{P}_i$ , and 3-aminopropylphosphonate, 3-APP, respectively) were transformed into pH curves using established algorithms. While  $\text{P}_i$  is an endogenous compound, 3-APP had to be injected intraperitoneally. Then, we developed algorithms for the calculation of six to eight quantitative pH parameters from the digital points of each pH curve obtained. For this purpose, each pH distribution profile was approximated as a histogram, and intensities were corrected for the nonlinearity between chemical-shift and pH. For each histogram derived from a  $\text{P}_i$  or 3-APP resonance, we obtained the following tumor pH profile parameters: weighted mean, weighted median, mode(s), skewness (asymmetry), kurtosis (peakedness), and entropy (smoothness). In addition, relative sizes of tissue volumes defined by characteristic pH ranges were estimated by integration and/or by fitting the curve to multiple modes. Our algorithms and the results obtained for animal models were validated (i) by computer simulations of  $^{31}\text{P}$  NMR resonances and pH profiles; and (ii) by comparison with combinations of  $\leq 3$  test solutions at well-defined pH values, containing the pH reporter molecule 3-APP. All calculations were performed with an EXCEL spreadsheet, thus avoiding any specialized software or hardware. Consequently, heterogeneous  $\text{pH}_i$  and  $\text{pH}_e$  distribution profiles in tumors can be characterized by multiple quantitative parameters derived from classical statistics, through histograms obtained from *in vivo*  $^{31}\text{P}$  NMR spectra. This original technique is helpful in analyzing tumor tissue features

with increased detail, based on a single experiment also yielding information on underlying energy and phospholipid metabolism.

**Keywords:**

Tissue pH distribution statistics

Quantitation of tumor pH heterogeneity

Intracellular and extracellular pH

In vivo  $^{31}\text{P}$  NMR spectroscopy

Skewness and kurtosis of pH distributions

## INTRODUCTION

In physiological tissues, the interplay of metabolism, ion transport and pH buffering results in efficient pH regulation. The presence of macroscopic and microscopic membrane structures, such as the basement membrane and various cell membranes, permits the coexistence of multiple tissue compartments characterized by different pH values. This highlights the necessity to not only measure average tissue pH values, but to quantitatively assess pH heterogeneity. Although non-invasive determination of intra and extracellular pH ( $\text{pH}_i$  and  $\text{pH}_e$ ) in mammals, notably by way of nuclear magnetic resonance (NMR) techniques, has become more common in recent years, there is at present no method that provides quantitative parameters specifically characterizing the *heterogeneity* of  $\text{pH}_i$  and  $\text{pH}_e$  in a given tissue volume. Yet, there is a genuine need for such measurements as a variety of pathologies (cancer and inflammation, among others) are associated with heterogeneous pH regulation (1-3). Even normal activity such as muscle exercise can generate complex tissue pH distributions as a function of biological characteristics (4). To address this challenge, we have developed a new approach based on multiparametric analysis of non-invasive *in vivo*  $^{31}\text{P}$  NMR spectra.

The proposed strategy is based on the circumstance that pH-sensitive magnetic resonance spectroscopy (MRS) signals from heterogeneous tissues represent entire pH distributions (pH profiles), rather than merely providing one "typical"  $\text{pH}_i$  or  $\text{pH}_e$  value. Since pH reporter molecules are electrically charged, they cannot freely cross membranes. This has a twofold consequence: pH reporter molecules do not move freely (i) between the intracellular and the extracellular space, nor (ii) between extracellular spaces that are separated by a monolayer or a multilayer of cells. Thus, these molecules do not undergo exchange between microscopic tissue regions of different pH, and the pH-sensitive chemical shift of the detected nucleus is not averaged out in the course of an MRS experiment. In theory, a pH reporter may be exchanged between extracellular regions not separated by cells or membranes. This would lead to chemical-shift averaging (fast exchange), or to a situation analogous to the classical case of an intermediate chemical exchange rate regime

between two molecular species of different chemical shift. However, this type of fast or intermediate exchange should not play an important role in the case of tissue pH because tissue areas of different pH are usually separated by membranes, e.g. cell layers; otherwise the pH gradient would rapidly dissipate due to proton diffusion. We inject the pH<sub>e</sub> reporter molecule, 3-aminopropylphosphonate (3-APP), into the experimental animal prior to the MRS experiment. Then, <sup>31</sup>P NMR spectra are acquired under anesthesia, followed by evaluation of the 3-APP resonance for pH<sub>e</sub> analysis, and of the endogenous inorganic-phosphate (P<sub>i</sub>) resonance for pH<sub>i</sub> analysis (5). The use of the P<sub>i</sub> signal for pH<sub>i</sub> measurement was pioneered by Moon and Richards (6) for cell suspensions, and was further developed for *in vivo* application in rodent tumors (7). Later, this concept was complemented by the introduction of exogenous 3-APP for pH<sub>e</sub> measurement (8). Conventionally, the P<sub>i</sub> and 3-APP MR signals are converted to pH curves, and the highest point in each curve ("the" maximum) is interpreted to be "the" pH<sub>i</sub> or pH<sub>e</sub> value of the measured tissue volume (9). Although this procedure yields fairly realistic average pH values for narrow and symmetric pH distributions, it is inadequate when pH distributions deviate from this ideal shape due to significant pH heterogeneity within the measured volume (10). While others have previously noticed an influence of pH heterogeneity on the appearance of P<sub>i</sub> (4, 11) and 3-APP (8) spectral lines, we exploit here, for the first time, the resulting pH curve shapes to derive quantitative parameters characterizing the underlying distributions of pH values. In addition to one or multiple pH<sub>e</sub> and pH<sub>i</sub> modes (= pH<sub>e</sub> and pH<sub>i</sub> curve maxima, respectively), the most basic parameters are weighted means and weighted medians (12) for pH<sub>e</sub> and pH<sub>i</sub>, each of which takes into account the entire respective pH distribution. Further pH<sub>e</sub> and pH<sub>i</sub> lineshape parameters are obtained to characterize the asymmetry (skewness (13)), peakedness (kurtosis (12)) and smoothness (entropy (14, 15)) of pH distributions. Finally, ratios of areas under individual pH modes and/or ranges are determined to obtain a quantitative measure of the relative sizes of tissue volumes with different pH values. All parameters are based on suitably weighted digital points of pH curves derived from <sup>31</sup>P NMR spectra. A crucial aspect of our new paradigm is that these quantitative parameters describe global features of pH

heterogeneity within a selected tissue volume. None of the currently available *in vivo* tissue pH methods provides such parameters.

We apply our approach to experimental tumors that have previously shown a relationship between pH heterogeneity and the extent of tumor necrosis (16). We assess the validity of our approach (i) by means of computer simulating  $^{31}\text{P}$  NMR spectral lines, including thorough error analysis, and (ii) by way of *in vitro*  $^{31}\text{P}$  NMR experiments based on 3-APP solutions with well-defined pH values. These findings have significant implications for the study of the relationship between pH alterations and biological properties of tissue, *e.g.* tumor growth behavior and cancer cell death, but also for other pathologies associated with perturbations of pH regulation.

## **MATERIALS AND METHODS**

### **Animals, cancer cells and phantoms used**

Animal studies were in agreement with the French guidelines for animal care, and were approved by the Committee on Ethics of the University of Aix-Marseille. Pouysségur's laboratory obtained the CCL39 clone from ATCC in 1978. They then isolated from these chinese hamster lung fibroblasts mutants that have been very well characterized and published in PNAS and Nature. Since then these cell lines have been maintained in Pouysségur's laboratory and checked before each experiment for the specific mutation in the glycolytic-defective phenotype. Further details concerning our tumor model have been described elsewhere (16).

Aqueous solutions of the  $\text{pH}_e$  reporter compound, 3-APP were prepared at different concentrations, and were adjusted to appropriate pH values with HCl and NaOH solutions. Since tissue  $\text{pH}_e$  heterogeneity is by far more pronounced and prevalent than  $\text{pH}_i$  heterogeneity, we decided to focus our phantom experiments on 3-APP solutions. However, the validation obtained for 3-APP in this study can be generalized to  $\text{P}_i$  since pH sensitivities and relevant  $\text{pK}_a$  values are only slightly different between these two compounds (Section S1.1). First, three 245-mM 3-APP solutions were prepared at pH 7.45, 7.00 and 6.50. These

solutions were then serially diluted by a factor of 1.5, then 2, between subsequent  $^{31}\text{P}$  NMR measurements.

These solutions were transferred to 5-mm NMR tubes (528-PP) from Wilmad (Vineland, NJ, USA), cut to size (length ca. 4 cm) to suit the spatial conditions of the NMR probe described below (see also Section S2.1). Up to three of these shortened NMR tubes were inserted into the cap of a shortened 50-mL centrifuge tube (Corning; Fisher Scientific, Illkirch, France) filled with saline. In addition, a 50 mM 3-APP solution (free acid dissolved in  $\text{D}_2\text{O}$ ) was prepared. This solution was then transferred to (i) a standard size 5-mm NMR tube (528-PP), and (ii) a glass sphere (1 cm diameter).

### **Acquisition of $^{31}\text{P}$ NMR spectra and proton images of tumors and phantoms**

Mouse tumors were measured *in-vivo* as described previously (16). For phantom measurements, the spherical phantom, or the centrifuge tube cone filled with saline and with one to three NMR tubes containing 3-APP solution, was placed on the same one-turn  $^{31}\text{P}$  surface coil used for *in-vivo* measurements, mounted in the same proton volume coil (16). The NMR spectrometer/imager employed for both phantoms and tumors was a BIOSPEC 47/40 system (4.7 T; Bruker, Wissembourg, France).  $^{31}\text{P}$  NMR spectra were acquired using a pulse-acquire sequence with volume selection based on outer-volume suppression (OVS) (17). To obtain the fine structure of the 3-APP spectrum under ideal conditions, high-resolution  $^{31}\text{P}$  NMR spectroscopy of the 50 mM 3-APP solution in 5-mm NMR tubes was performed on an AVANCE 400 spectrometer (Bruker) at 9.4 T equipped with a quadronuclear probe (QNP) by way of a standard pulse-acquire sequence (18-20), with and without proton decoupling.

### **Processing of tumor and phantom $^{31}\text{P}$ NMR spectra**

$^{31}\text{P}$  NMR free induction decays (FID) were Fourier-transformed after zero-filling and multiplication with appropriate Lorentzian-Gaussian functions (XWINNMR software, Bruker). The chemical-shift values of the processed  $^{31}\text{P}$  NMR spectra (21) were then converted to pH.

After intensity corrections, the resulting data sets served as histograms (22) for the determination of weighted-average pH (mean pH), weighted median pH, skewness, kurtosis and entropy (23-26). In addition, individual modes were determined. For pH distributions permitting the distinction of two or more characteristic pH ranges, the areas under the individual pH ranges or modes were quantitated by two different methods: (i) integration, and (ii) curve fitting employing the MDCON ("mixed deconvolution") function in Bruker's TopSpin software. Finally, these evaluation methods were applied to *in vivo*  $^{31}\text{P}$  NMR signals of 3-APP in mouse tumor xenografts (16). High-resolution  $^{31}\text{P}$  NMR spectra of 3-APP solutions were processed using Bruker's TopSpin software. Further NMR processing details, as well as the theoretical background and the algorithms used for the calculation of pH heterogeneity parameters are presented in Sections S1 and S2. The EXCEL spreadsheet pH\_param\_template.xlsx provided by us is, in effect, a computer program; it serves both as an example of our calculations and as a template for use by interested researchers. This EXCEL file can be downloaded using the URL address [http://crmbm.univ-amu.fr/homepage/nlutz/pH\\_param\\_template.xlsx](http://crmbm.univ-amu.fr/homepage/nlutz/pH_param_template.xlsx). An option to use the results of lineshape deconvolution for better definition of inorganic phosphate ( $\text{P}_i$ ) lines is included in the algorithms implemented in this template.

### ***In silico* calculations**

The purpose of our *in silico* calculations is fourfold: (i) to test, based on well-defined Gaussian pH distributions, the validity of our algorithms; (ii) to explore the effects of ppm-to-pH conversion on the symmetric shapes of two distinct Gaussian 3-APP  $^{31}\text{P}$  NMR spectral lines; (iii) to study the statistical parameters characterizing the overall pH distributions resulting from the addition, in varying proportions, of the two pH curves generated in (ii); and (iv) to compare simulated, phantom and *in-vivo* pH heterogeneity parameter values.

As a consequence of the nonlinearity of the ppm-to-pH conversion, a pH lineshape may significantly deviate from its underlying chemical-shift lineshape. We generated two Gaussian curves with a chemical-shift abscissa scaled such that, following ppm-to-pH

conversion, the centers of the curves fell upon pH 6.5 and 7.2. These values as well as the associated linewidths were chosen to be close to values commonly found for  $pH_e$  in *in vivo* experiments. The resulting (asymmetric) pH curves were then used to characterize these simulated pH distributions by means of statistical pH distribution parameters. Conversely, we generated in an EXCEL spreadsheet Gaussian pH curves centered about pH 6.5 and 7.2. Based on these curves we backward simulated the corresponding 3-APP line, and studied the asymmetry effects that (symmetric) Gaussian pH distribution parameters would undergo after conversion to simulated 3-APP resonances. Finally, two computer-generated Gaussian curves were added to model bimodal (27) pH distributions for statistical analysis.

## RESULTS

### Generation of bimodal pH profiles corrected for the nonlinearity between the chemical-shift and pH scales

The effects of converting the ppm scale of the 3-APP spectrum to a pH scale were first studied for a bimodal pH distribution from a mouse tumor xenograft (Fig. 1 A). Most heterogeneous tumors feature irregularly shaped pH distributions rather than strictly bimodal or multimodal patterns (16). However, to validate our method we primarily focused on bimodal and trimodal pH distributions, because the concept of quantitative pH heterogeneity parameters is best tested and verified on the basis of models representing well-defined pH distribution functions. Nevertheless, nearly all quantitative parameters suggested in this report are universally applicable to any given distribution of pH values; their use does not depend on the existence of distinct pH modes (see also following paragraph). Our results were first validated by using a phantom consisting of two NMR tubes filled with 3-APP solutions adjusted to pH 6.5 and 7.4 (Fig. 1 B and C). Uncorrected ppm-to-pH conversion (eq. S6, with intensity  $I_{3-APP}$  as in underlying NMR spectrum) renders the upper part of each pH mode narrower (Fig. 1, bottom row, dotted lines) than it is in the corresponding  $^{31}P$  NMR spectrum (Fig. 1, middle row). In addition, the outer wings of the pH curves do not descend

to the baseline, even for apparent pH values as high as 8.5, or as low as 5.5. However, such extreme pH values are unlikely to exist in tumors and most mammalian tissues, and are unquestionably the result of a systematic artifact. This artifact is remedied (28) by applying an intensity correction for the nonlinear relationship between the chemical-shift and pH scales (eq. S8). Following this correction, pH lineshapes are further narrowed, and the outer wings of both modes return to the baseline within the displayed pH range (Fig. 1, bottom row, solid lines). It is evident that omitting this correction step would yield biased and excessively broad pH distributions by overemphasizing both extremely high and low pH values, due to their large difference from the  $pK_{a2}$  of 3-APP. Obviously, including this nonlinearity correction is even more critical in the evaluation of a heterogeneous pH profile than it is for the determination of a single tissue pH value based on the global maximum of a pH curve (9). Also note that each mode (= maximum of each peak) is shifted between the spectral line and the pH curve, and is slightly different between corrected and uncorrected pH curves (Fig. 1 A - C). The latter effect has been previously observed for pH curves with a single maximum (9). For best comparison between phantom and *in vivo* studies, the processing parameters for phantom spectra (Fig. 1 B) were judiciously chosen to yield pH curves whose shapes resemble pH curves obtained for heterogeneous tissue (Fig. 1 A). Even so, stronger filtering parameters (typically GB = 0.007, LB = -25 Hz) were needed for phantom spectra than for tissue spectra (typically GB = 0.01, LB = -20 Hz) because the magnetic-field inhomogeneity is intrinsically lower in phantoms than in tissue. For phantom-derived and computer-simulated pH distributions, the "e" (or "i") index indicates that the pH modes in question are linked to the chemical shift of 3-APP (or  $P_i$ ) signals, and have been chosen with the intention to compare these modes with similar extracellular (or intracellular) pH distribution modes detected in the tumors of 3-APP-injected animals.

### **<sup>31</sup>P NMR spectra yield up to eight quantitative pH distribution parameters**

It is highly desirable to provide quantitative parameters to characterize tissue heterogeneity with respect to pH. The number of quantitative parameters that can be obtained from a <sup>31</sup>P

NMR spectroscopy-based analysis of pH heterogeneity is a function of the pH curve shape. The following six parameters can be extracted from virtually any pH curve: (i)  $pH_{\max}$ , the global maximum of the pH curve (classical  $^{31}\text{P}$  NMR method); (ii)  $\overline{pH}$ , the weighted-average (mean) pH; (iii)  $\widetilde{pH}$ , the weighted median pH; (iv) skewness; (v) kurtosis; (vi) entropy (the underlying theory and algorithms are explained in great detail in Section S1). For a pH profile that suggests the presence of multiple distinct pH ranges, a characteristic pH value can be obtained for each of these ranges by employing methods (i) to (iii). The relative weight of each of these pH ranges can be calculated by (vii) separately integrating the area under the curve for each individual pH range, followed by calculating ratios of these areas. For multimodal pH profiles that are amenable to numerical fitting of analytical curves, (viii) pH values for multiple maxima or modes ( $pH_1, pH_2 \dots$ ), and (ix) areas under individual fitted modes can be obtained as results of the fitting procedure. Alternatively, multiple maxima corresponding to method (viii) can be directly read out by (x) visual inspection or, for more precision, (xi) a software module based on interpolation (such as Bruker's peak picking routine), while the areas for these pH modes can be integrated as described above under (vii).

In the interpretation of pH curves derived from  $^{31}\text{P}$  NMR spectra, spectral line broadening due to magnetic-field inhomogeneity, spectral processing (filtering) and phosphorus-proton J coupling (for 3-APP), and, to a much lesser extent,  $T_2$  processes should be taken into account. In fact, the standard error and width of a  $^{31}\text{P}$  NMR-derived pH curve, or of an individual mode within a pH curve, would somewhat overstate the pH range actually present in the sample; for this reason, they are not included in the list of parameters above. Obviously, kurtosis, a measure of the peakedness of a distribution, represents the true pH distribution function more faithfully to the extent that the influence of lineshape effects unrelated to pH can be minimized as described in Sections S1.2.1 and S1.2.11.

Quantification of pH heterogeneity by statistical parameters was studied based on pH distributions *in vivo* (mouse tumor models), *in vitro* (phantom models), and *in silico* (computer models). *In vivo* and *in vitro* results are presented in the following paragraphs, whereas

findings of computer simulations are provided in Tables S2 and S3; in Figure S2 panels E and F; and in Figure S4.

### Quantification of unimodal pH distributions

We first tested our algorithms for a unimodal pH distribution in a phantom containing a 3-APP solution at pH = 7.00. Owing to the perfect pH homogeneity in this sample the resulting pH distribution curve was very symmetric (Fig. 2 A). As a consequence, weighted mean ( $\overline{\text{pH}}_e$ ), weighted median ( $\widetilde{\text{pH}}_e$ ) and mode ( $\text{pH}_{e1}$ ) had identical values (Table 1 A); compare also with computer-simulated results presented in Table S2. The small values obtained for skewness (G1) and kurtosis (G2) in this example suggest a nearly Gaussian pH curve. In fact, the  $^{31}\text{P}$  NMR lineshape obtained from a homogeneous 3-APP solution after strong Gaussian filtering has a considerable Gaussian character, and its symmetry is largely preserved in ppm-to-pH conversion if pH approximates the  $\text{pK}_{a2}$  of 3-APP. Also the entropy (H) of this pH distribution, indicating its smoothness, was smaller for this example than for any other example studied in this study. The unimodal  $\text{pH}_e$  distribution in a relatively homogeneous mouse tumor (Fig. 2 E) was more asymmetric than the pH distribution in Fig. 2 A, the left tail (low  $\text{pH}_e$ ) being heavier than the right tail (high  $\text{pH}_e$ ). Therefore  $\overline{\text{pH}}_e < \widetilde{\text{pH}}_e < \text{pH}_{e2}$ , and the  $\text{pH}_e$  distribution showed a negative skew (G1) (Table 1 E). While this  $\text{pH}_e$  distribution was more leptokurtic (increased G2) than that of Table 1 A, it also had a higher entropy reflecting a more even distribution. In tumors, the intracellular pH is generally more homogeneous than the extracellular pH (16);  $\text{pH}_i$  values are distributed over a considerably smaller range than  $\text{pH}_e$  values. Bi- or multimodal  $\text{pH}_i$  distributions are rare (Fig. 3 A) whereas most tumors exhibit more or less asymmetric unimodal  $\text{pH}_i$  distributions (Fig. 3 B), occasionally presenting a shoulder (Fig. 3 C and D). The narrowest unimodal  $\text{pH}_i$  distribution (Fig. 3 B) was the most leptokurtic and the least smooth  $\text{pH}_i$  distribution (Table 2 B). Owing to its high asymmetry reflected by its skewness, the differences between  $\text{pH}_{i1}$ ,  $\overline{\text{pH}}_i$  and  $\widetilde{\text{pH}}_i$  were rather large. In summary, all six

quantitative parameters applicable to unimodal distributions describe the behavior of the underlying phantom and tissue samples very well, for both  $\text{pH}_e$  and  $\text{pH}_i$ .

### **The number of distinct pH environments in a sample can be modeled by phantom $^{31}\text{P}$ NMR experiments**

In addition to the universally accessible parameters described in the preceding paragraph, some  $^{31}\text{P}$  NMR-based pH profiles reveal a finite number of distinct pH environments. Note that no assumptions are made with respect to the size and spatial distribution of the underlying tissue volume elements. The capability of 3-APP  $^{31}\text{P}$  NMR spectra to reveal multimodal pH heterogeneity was tested by studying phantoms that contained one to three compartments filled with 3-APP solutions of varying pH. As a starting point, a non-decoupled high-resolution  $^{31}\text{P}$  NMR spectrum of an 3-APP solution was obtained (Fig. 4 A). Then, a 3-APP solution contained in a spherical phantom was measured in a small-animal NMR spectrometer/imager. Under these conditions, the  $^{31}\text{P}$  NMR peaks were broadened such that only five broad 3-APP peaks could be distinguished (Fig. 4 B). Subsequently, a glass sphere phantom similar to the phantom used for Fig. 4 B (with pH adjusted to pH 7.0) was imaged (Fig. 4 C). The quality of the 3-APP spectrum from the selected volume presented in Fig. 4 C was comparable to the quality of the spectrum shown in Fig. 4 B. However, major filtering had been applied to increase the final linewidth of the pH curve to a value close to what is achievable *in vivo*, such that the multiplet was no longer resolved (Fig. 4 F). Next, phantoms containing two and three NMR tubes were imaged (Figs. 4 D and E, respectively). These tubes were immersed in saline, and contained 3-APP solutions at about pH 6.50 and 7.45 (Fig. 4 D), and at about pH 6.50, 7.00 and 7.45 (Fig. 4 E). All 3-APP concentrations were kept at roughly the same order of magnitude to prevent the bases of larger peaks from hiding considerably smaller peaks. The corresponding spectra exhibited two (Fig. 4 G) and three (Fig. 4 H) components (modes) respectively. This measurement series demonstrates that under ideal conditions, up to three distinct regions of similar size can be identified based on

differing pH values, for a pH range close to physiological values. See Section S1.2.8 for further details.

### **The sensitivity of *in vivo* $^{31}\text{P}$ NMR spectroscopy in identifying multiple distinct pH environments can be modeled by phantom experiments**

The ability of 3-APP  $^{31}\text{P}$  NMR spectra to identify distinct sample regions by their pH values not only depends on the number of such regions and on the pH differences between these regions, but also on the relative intensities of the pH modes associated with these regions. We mimicked variations in relative volumes within a tissue region by varying the 3-APP concentration in one of the two NMR tubes of the phantom used. The two pH values chosen were about pH 6.50 and 7.45. The acidic solution was diluted to approximately half the concentration of the alkaline solution. Then, serial dilutions were prepared for the acidic solution as described in the MATERIALS AND METHODS section, and a  $^{31}\text{P}$  NMR spectrum was acquired after each dilution step. The qualitative results of these measurements are presented here whereas the quantitative results can be found in Table S1. The corresponding pH curves (Figs. 4 I - L) show a readily identifiable  $\text{pH}_{\text{e}2}$  mode for a peak height that is roughly of the same order (64%) as the  $\text{pH}_{\text{e}1}$  peak height (Fig. 4 I). However, after the third dilution step, with the  $\text{pH}_{\text{e}2}$  peak height being roughly 8% of the  $\text{pH}_{\text{e}1}$  peak height, the  $\text{pH}_{\text{e}2}$  mode was hardly detectable, despite a difference of *ca.* 0.8 pH units between the two compartments (Fig. 4 L). In an *in vivo* situation where the corresponding lines are somewhat broader and noisier, the  $\text{pH}_{\text{e}2}$  peak height would need to be at least approximately 20% of the  $\text{pH}_{\text{e}1}$  peak height for an evaluable  $\text{pH}_{\text{e}2}$  mode.

### **Quantification of bimodal and multimodal pH distributions**

Two basic forms of bimodal pH distributions were studied in phantoms and mouse tumors. In the first type, both modes resulted in maxima of similar heights (Fig. 2 B and F); in the second type, one mode was significantly more pronounced than the other (Fig. 2 C and G). Although both modes in Fig. 2 B were of comparable height, the distribution pattern was not

symmetric as the areas under the two peaks were different; the  $\text{pH}_{e2}$  area was roughly three quarters the  $\text{pH}_{e1}$  area (Table 1 B). Almost identical area ratios were measured by two different methods: (i) integration based on the weights of digital curve points, and (ii) deconvolution based on fitted Gaussian/Lorentzian functions (29).

The pH distribution asymmetry for the phantom described in Table 1 B lead to a difference of 0.17 pH units between  $\overline{\text{pH}}_e$  and  $\widetilde{\text{pH}}_e$ . The  $\text{pH}_{e1}$  and  $\text{pH}_{e2}$  modes were well separated due to the large difference of approximately 0.9 pH units (Fig. 2 B). By contrast, the two modes in the tumor  $\text{pH}_e$  distribution (Fig. 2 F) exhibited more overlap as their pH difference was only approximately 0.6 pH units (Table 1 F). Since in the latter example the areas under the two modes were almost identical (ratio close to unity), the  $\text{pH}_e$  distribution was nearly symmetrical and, as a consequence, the difference between  $\overline{\text{pH}}_e$  and  $\widetilde{\text{pH}}_e$  was virtually negligible (Table 1 F). For the examples plotted in Fig. 2 C and G, the overlapping modes were characterized by similar area ratios;  $\text{pH}_{e2}/\text{pH}_{e1} \approx 0.4$  for the former (Table 1 C), and  $\text{pH}_{e1}/\text{pH}_{e2} \approx 0.5$  for the latter (Table 1 G). As was to be expected from these asymmetries,  $\widetilde{\text{pH}}_e$  was greater than  $\overline{\text{pH}}_e$  (Table 1 C), and smaller than  $\overline{\text{pH}}_e$  (Table 1 G), respectively, by the same amount (approximately 0.1 pH units). The superimpositions of the two pH curve modes were comparable because the differences between  $\text{pH}_{e1}$  and  $\text{pH}_{e2}$  were similar (approximately 0.8 and 0.7 pH units, respectively). Although these relative area ratios represent relative tissue volumes, pH heterogeneity should not be confounded with morphological heterogeneity. An example of the latter is illustrated in *in vivo* images obtained by a  $T_1$ -weighted MRI sequence, for all tumors whose pH profiles are presented in this report (Fig. 5). It is obvious from these cross sections that the glycolysis-deficient variant, CCL39/gly<sup>-</sup> (Fig. 5 A and B), showed less morphological heterogeneity, notably less necrosis, than most wild-type tumors, CCL39 (Fig. 5 C - F). Nonetheless, even relatively homogeneous appearing tumors may produce clearly heterogeneous pH profiles (Figs. 2 G and 3 A, corresponding to Fig. 5 G and B, respectively).

The concepts of skewness, kurtosis and entropy are mostly employed to characterize unimodal probability distributions (30). However, they can also reveal global characteristics of pH profiles with more than one mode. For instance, the nearly symmetric modes displayed in Fig. 2 B result in vanishing skewness (Fig. 2 B), whereas the strong asymmetries indicated by modes of unequal peak heights (Fig. 2 C and G) resulted in negative and positive  $G_1$  values as shown in Table 1 C and G, respectively. Two examples of trimodal  $pH_e$  distributions were analyzed. The three modes from our phantom could be quantified relatively easily (Fig. 2 D). However, *in vivo* situations amenable to precise quantification of three separate modes are rare; we present here an example (Fig. 2 H) in which one mode ( $pH_{e1}$ ) appears as a shoulder on another mode ( $pH_{e3}$ ). Further details concerning the evaluation of bi- and multimodal pH distributions are given in Section S1.2.10. A flowchart displaying all basic steps required for our pH parameter calculations is given in Figure S6.

## DISCUSSION

This report describes the first method providing quantitative heterogeneity parameters that characterize the statistical distribution of tissue pH values. The approach presented here can be extended to further statistical parameters describing the shape of pH distributions (pH profiles). In fact, besides skewness, kurtosis and entropy, statistics provides a number of parameters that characterize distribution functions, each one presenting specific advantages and disadvantages (31). An original characteristic of our approach is that it provides multiple quantitative parameters describing global features of pH heterogeneity within a selected tissue volume. These parameters describe details concerning the exact shape of pH distributions. None of the current methods designed to assess spatial pH differences in tissues *in vivo* provides such parameters. For instance, fluorescence imaging microscopy using a pH-sensitive fluorophore (32) is able to detect pH variations with submillimeter resolution (1, 33), but as an optical method this approach is restricted to tissue surfaces. Proton-based NMR methods such as chemical-shift imaging (CSI) of exogenous  $pH_e$  (but *not*

pH<sub>i</sub>) markers are well established (34, 35); however, their applications have essentially been limited to distinguishing pH<sub>e</sub> values in a viable tumor rim from those of tumor tissue close to necrosis in two-dimensional pH charts. More recent pH<sub>e</sub> mapping techniques based on pH-sensitive relaxation (36), chemical exchange saturation transfer (CEST) (37) or hyperpolarized <sup>13</sup>C CSI (38) offer somewhat better spatial resolution than <sup>1</sup>H CSI. However, besides being rather intricate, requiring special pulse sequences and/or lacking validated robustness, these techniques do not offer quantitative parameters characterizing the distribution of pH values. They may thus be considered complementary to the <sup>31</sup>P NMR method presented here. Our technique results in pH profiles indistinguishably taking into account both macroscopic and microscopic pH heterogeneity; therefore, the detection of pH heterogeneity is not limited to differences between tissue regions above a critical size. By contrast, MR images are voxel-based, and for this reason pH differences existing within a voxel (i.e., between tissue regions smaller than a voxel) are averaged and cannot be represented by image-based pH maps.

The method presented here allows simultaneous non-invasive characterization of complex *in vivo* pH<sub>i</sub> and pH<sub>e</sub> distributions. It opens important perspectives in many areas of biomedical research, either in animal models or in humans. Both intra and extracellular pH heterogeneity can be determined simultaneously in animal models, based on the <sup>31</sup>P NMR resonance of endogenous inorganic phosphate (P<sub>i</sub>) and exogenous 3-APP, respectively. As for other measured biological quantities, the pH parameters suggested here need to be evaluated in comparisons between groups of animals or humans to determine their respective roles in biological research. While at the present time human applications are limited to intracellular pH analysis (based on the P<sub>i</sub> signal), future development of extracellular phosphonated pH markers that are safe for human use should lead to an extension of this method to patient studies. In addition, the pH profiles presented in this report can be obtained with spatial resolution in cases where the use of appropriate <sup>31</sup>P NMR sequences (e.g., chemical shift imaging) is feasible (2). Finally, metabolic events frequently coupled with pH changes (notably hypoxia-induced energy (39) and phospholipid metabolism

(40)) can be analyzed from the very same  $^{31}\text{P}$  NMR spectrum obtained for pH analysis, and can be directly correlated with pH heterogeneity to analyze the metabolic underpinnings of variations in the pH parameters introduced here. In addition, the  $^{31}\text{P}$  NMR measurement can be combined seamlessly with other *in vivo* experiments in the same examination for further research into the physiopathological basis of pH heterogeneity, including both *in-vivo* and *in-vitro* metabolomics (41). For instance, the total pH heterogeneity determined by our new method (i.e., macroscopic and microscopic pH heterogeneity combined) may be used in conjunction with diffusion-weighted MRI results and spatially resolved pH maps to clarify to what extent structures underlying macroscopic diffusion tensor anisotropy (42) and pH variations explain the total pH heterogeneity found in tumors. Histological microscopy and other *ex-vivo* microscopy methods may reveal microscopic structures potentially contributing to the total tumor pH heterogeneity quantifiable by the method presented here.

## GRANT SUPPORT

Funding from CNRS (UMR 6612, 7339 and 6543) is gratefully acknowledged.

## References

1. Helmlinger, G., Yuan, F., Dellian, M., and Jain, R. K. Interstitial pH and pO<sub>2</sub> gradients in solid tumors in vivo: high-resolution measurements reveal a lack of correlation. *Nat Med*, **3**: 177-182, 1997.
2. Kobus, T., Bitz, A. K., van Uden, M. J., Lagemaat, M. W., Rothgang, E., Orzada, S., Heerschap, A., and Scheenen, T. W. In vivo 31P MR spectroscopic imaging of the human prostate at 7 T: safety and feasibility. *Magn Reson Med*, **68**: 1683-1695, 2012.
3. Vandeborne, K., McCully, K., Kakihira, H., Prammer, M., Bolinger, L., Detre, J. A., De Meirlier, K., Walter, G., Chance, B., and Leigh, J. S. Metabolic heterogeneity in human calf muscle during maximal exercise. *Proc. Natl. Acad. Sci. USA*, **88**: 5714-5718, 1991.
4. Rossiter, H. B., Ward, S. A., Howe, F. A., Kowalchuk, J. M., Griffiths, J. R., and Whipp, B. J. Dynamics of intramuscular 31P-MRS P(i) peak splitting and the slow components of PCr and O<sub>2</sub> uptake during exercise. *J Appl Physiol*, **93**: 2059-2069, 2002.
5. Ackerman, J. J., Soto, G. E., Spees, W. M., Zhu, Z., and Evelhoch, J. L. The NMR chemical shift pH measurement revisited: analysis of error and modeling of a pH dependent reference. *Magn Reson Med*, **36**: 674-683, 1996.
6. Moon, R. B. and Richards, J. H. Determination of intracellular pH by 31P magnetic resonance. *J Biol Chem*, **248**: 7276-7278, 1973.
7. Griffiths, J. R., Stevens, A. N., Iles, R. A., Gordon, R. E., and Shaw, D. 31P-NMR investigation of solid tumours in the living rat. *Biosci Rep*, **1**: 319-325, 1981.
8. Gillies, R. J., Liu, Z., and Bhujwalla, Z. M. 31P-MRS measurements of extracellular pH of tumors using 3-aminopropylphosphonate. *Am. J. Physiol.*, **36**: C195-C203, 1994.
9. Raghunand, N. Tissue pH measurement by magnetic resonance spectroscopy and imaging. *Methods Mol Med*, **124**: 347-364, 2006.
10. Madden, A., Glaholm, J., and Leach, M. O. An assessment of the sensitivity of in vivo 31P nuclear magnetic resonance spectroscopy as a means of detecting pH heterogeneity in tumours: a simulation study. *Br J Radiol*, **63**: 120-124, 1990.
11. Viola, A., Lutz, N. W., Maroc, C., Chabannon, C., Julliard, M., and Cozzone, P. J. Metabolic effects of photodynamically induced apoptosis in an erythroleukemic cell line. A (31)P NMR spectroscopic study of Victoria-Blue-BO-sensitized TF-1 cells. *Int J Cancer*, **85**: 733-739, 2000.
12. Sokal, R. R. and Rohlf, F. J. *Biometry*, 3rd edition. New York: Freeman, 1995.
13. Doane, D. P. and Seward, L. E. Measuring Skewness: A Forgotten Statistic? *J Stat Educ*, **19**: 1-18, 2011.
14. Cover, T. M. and Thomas, J. A. *Elements of information theory*. New York: Wiley, 1991.
15. Lesne, A. Statistical entropy: at the crossroads between probability, information theory, dynamical systems and statistical physics. *Math. Struct. Comp. Sci.*, *in press*.
16. Chiche, J., Fur, Y. L., Vilmen, C., Frassinetti, F., Daniel, L., Halestrap, A. P., Cozzone, P. J., Pouyssegur, J., and Lutz, N. W. In vivo pH in metabolic-defective Ras-transformed fibroblast tumors: Key role of the monocarboxylate transporter, MCT4, for inducing an alkaline intracellular pH. *Int J Cancer*, **130**: 1511-1520, 2012.
17. Sauter, R., Mueller, S., and Weber, H. Localization in in vivo 31P NMR spectroscopy by combining surface coils and slice-selective saturation. *J. Magn. Reson.*, **75**: 167-173, 1987.
18. Lutz, N. W. and Cozzone, P. J. Multiparametric optimization of (31)P NMR spectroscopic analysis of phospholipids in crude tissue extracts. 1. Chemical shift and signal separation. *Anal Chem*, **82**: 5433-5440, 2010.
19. Lutz, N. W. and Cozzone, P. J. Multiparametric optimization of (31)P NMR spectroscopic analysis of phospholipids in crude tissue extracts. 2. Line width and spectral resolution. *Anal Chem*, **82**: 5441-5446, 2010.
20. Lutz, N. W. and Cozzone, P. J. Phospholipidomics by phosphorus nuclear magnetic resonance spectroscopy of tissue extracts. *In*: N. W. Lutz, J. V. Sweedler, and R. A. Wevers (eds.), *Methodologies for metabolomics*, pp. 377-414. New York: Cambridge University Press, 2013.

21. Le Fur, Y., Nicoli, F., Guye, M., Confort-Gouny, S., Cozzone, P. J., and Kober, F. Grid-free interactive and automated data processing for MR chemical shift imaging data. *Magma*, *23*: 23-30, 2010.
22. He, K. and Meeden, G. Selecting the number of bins in a histogram: A decision theoretic approach. *J Stat Plan Inference*, *61*: 49-59, 1997.
23. Hargas, L., Koniar, D., and Stofan, S. Sophisticated biomedical tissue measurement using image analysis and virtual instrumentation. In: S. Folea (ed.), *Practical applications and solutions using Labview™ software*. Rijeka: InTech, 2011.
24. Kohler, U. and Kreuter, F. *Data analysis using stata*. College Station: Stata Press, 2005.
25. Frigg, R. and Wernndl, C. Entropy: A Guide for the Perplexed. In: C. Beisbart and S. Hartmann (eds.), *Probabilities in physics*. Oxford: Oxford University Press, 2011.
26. Güçlü, B. Maximizing the entropy of histogram bar heights to explore neural activity: a simulation study on auditory and tactile fibers. *Acta Neurobiol Exp*, *65*: 399-407, 2005.
27. Park, H. M. *Univariate Analysis and Normality Test Using SAS, Stata, and SPSS*. Bloomington: The University Information Technology Services (UITSS) Center for Statistical and Mathematical Computing, Indiana University, 2008.
28. Graham, R. A., Taylor, A. H., and Brown, T. R. A method for calculating the distribution of pH in tissues and a new source of pH error from the 31P-NMR spectrum. *Am J Physiol*, *266*: R638-645, 1994.
29. Marshall, I., Higinbotham, J., Bruce, S., and Freise, A. Use of Voigt lineshape for quantification of in vivo 1H spectra. *Magn Reson Med*, *37*: 651-657, 1997.
30. Jensen, P. A. and Bard, J. F. *Operations Research Models and Methods Vol. Supplementary material* <http://www.me.utexas.edu/~jensen/ORMM>. Hoboken, NJ, USA: Wiley, 2003.
31. DeCarlo, L. T. On the meaning and use of kurtosis. *Psychol. Methods*, *2*: 292-307, 1997.
32. Lin, Y., Wu, T. Y., and Gmitro, A. F. Error analysis of ratiometric imaging of extracellular pH in a window chamber model. *Journal of biomedical optics*, *17*: 046004, 2012.
33. Hak, S., Reitan, N. K., Haraldseth, O., and de Lange Davies, C. Intravital microscopy in window chambers: a unique tool to study tumor angiogenesis and delivery of nanoparticles. *Angiogenesis*, *13*: 113-130, 2010.
34. Garcia-Martin, M. L., Herigault, G., Remy, C., Farion, R., Ballesteros, P., Coles, J. A., Cerdan, S., and Ziegler, A. Mapping extracellular pH in rat brain gliomas in vivo by 1H magnetic resonance spectroscopic imaging: comparison with maps of metabolites. *Cancer Res*, *61*: 6524-6531, 2001.
35. Provent, P., Benito, M., Hiba, B., Farion, R., Lopez-Larrubia, P., Ballesteros, P., Remy, C., Segebarth, C., Cerdan, S., Coles, J. A., and Garcia-Martin, M. L. Serial in vivo spectroscopic nuclear magnetic resonance imaging of lactate and extracellular pH in rat gliomas shows redistribution of protons away from sites of glycolysis. *Cancer Res*, *67*: 7638-7645, 2007.
36. Garcia-Martin, M. L., Martinez, G. V., Raghunand, N., Sherry, A. D., Zhang, S., and Gillies, R. J. High resolution pH(e) imaging of rat glioma using pH-dependent relaxivity. *Magn. Reson. Med.*, *55*: 309-315, 2006.
37. Liu, G., Li, Y., Sheth, V. R., and Pagel, M. D. Imaging In Vivo Extracellular pH with a Single Paramagnetic Chemical Exchange Saturation Transfer Magnetic Resonance Imaging Contrast Agent. *Mol Imaging*, *11*: 47-57, 2012.
38. Gallagher, F. A., Kettunen, M. I., and Brindle, K. M. Imaging pH with hyperpolarized 13C. *NMR Biomed*, *24*: 1006-1015, 2011.
39. Vaupel, P., Kallinowski, F., and Okunieff, P. Blood flow, oxygen and nutrient supply, and metabolic microenvironment of human tumors: a review. *Cancer Res*, *49*: 6449-6465, 1989.
40. Glunde, K., Shah, T., Winnard, P. T., Jr., Raman, V., Takagi, T., Vesuna, F., Artemov, D., and Bhujwala, Z. M. Hypoxia regulates choline kinase expression through hypoxia-inducible factor-1 alpha signaling in a human prostate cancer model. *Cancer Res*, *68*: 172-180, 2008.
41. Lutz, N. W., Sweedler, J. V., and Wevers, R. A. (eds.) *Methodologies for metabolomics*. New York: Cambridge University Press, 2013.
42. Lope-Piedrafita, S., Garcia-Martin, M. L., Galons, J. P., Gillies, R. J., and Trouard, T. P. Longitudinal diffusion tensor imaging in a rat brain glioma model. *NMR in biomedicine*, *21*: 799-808, 2008.

## Figure legends

Figure 1. Examples of 3-APP  $^{31}\text{P}$  NMR spectra revealing pH heterogeneity in tissue and in a phantom.

A) CCL39 tumor xenograft in a mouse model. B) and C) Phantom consisting of two NMR tubes filled with 3-APP solutions at pH 6.5 and 7.4.

Top row: Representative MRI cross section through phantom or mouse tumor. Shaded areas in image indicate regions saturated by OVS during subsequently performed localized  $^{31}\text{P}$  NMR spectroscopy.

Middle row: spectra processed with Lorentzian-Gaussian lineshape transformation at GB = 0.01 and LB = -20 Hz (A), or at GB = 0.007 and LB = -25 Hz (B); or with apodization at LB = 15 Hz (C).

Bottom row: pH profiles derived from the spectra displayed in the top row. Dotted lines: uncorrected pH curves. Solid lines: pH curves with intensities corrected for the nonlinear relationship between chemical-shift and pH scales. In both tumor tissue and phantom, pH profiles exhibit a bimodal pH distribution pattern, with modes being centered about approximately pH 6.5 (left curve maxima,  $\text{pH}_{e2}$ ) and 7.4 (right curve maxima,  $\text{pH}_{e1}$ ).

Figure 2. Series of pH profiles derived from 3-APP  $^{31}\text{P}$  NMR resonances of phantoms and mouse tumors for varying numbers of characteristic  $\text{pH}_e$  values

A) - D) Typical shapes of pH profiles of 3-APP phantoms with one to three characteristic  $\text{pH}_e$  values.

E) - H) Typical shapes of  $\text{pH}_e$  profiles from 3-APP-injected mouse tumors with one to three characteristic  $\text{pH}_e$  values.

Vertical dashed lines in pH curves indicate the borderline between distinct pH regions within each pH profile, used for the integration of separate areas for the  $\text{pH}_{e1}$ ,  $\text{pH}_{e2}$  and  $\text{pH}_{e3}$  regions.

I) - L) Representative MRI cross sections of the tumors presenting the pH profiles given in E) - H). Shaded areas in images indicate regions saturated by OVS during subsequently performed localized  $^{31}\text{P}$  NMR spectroscopy.

Figure 3. Representative MRI cross sections and associated pH profiles derived from  $\text{P}_i$   $^{31}\text{P}$  NMR resonances of mouse tumors for varying numbers of characteristic  $\text{pH}_i$  regions.

A) - C) In almost all tumors,  $\text{pH}_i$  values were distributed over a considerably smaller pH range than  $\text{pH}_e$  values. Bi- or multimodal distributions as shown in (A) were rare.

D) Atypical case of a tumor  $\text{pH}_i$  distribution with a relatively heavy positive tail.

Vertical dashed lines in pH curves indicate the borderlines between distinct pH regions within each pH profile, used for the integration of separate areas under the  $\text{pH}_{i1}$  and  $\text{pH}_{i2}$  regions. Shaded areas in images indicate regions saturated by OVS during subsequently performed localized  $^{31}\text{P}$  NMR spectroscopy.

Figure 4.  $^{31}\text{P}$  NMR spectra, pH profiles and  $^1\text{H}$  MR images of 3-APP solutions

A) A high-resolution spectrum of an aqueous 3-APP solution in a 5-mm NMR tube, obtained at 160 MHz and Fourier transformed without filtering. The triple triplet and its associated proton-phosphorus coupling constants are indicated above the spectrum.

B) Spectrum of the same 3-APP solution as for (A), but contained in a 1-cm diameter glass sphere and acquired at 80 MHz on a 4.7 T MR imager/spectrometer. The chemical-shift range shown was adjusted such that the multiplet of this spectrum is aligned with the multiplet from (A).

C) Image of the phantom used for spectrum (B) and pH profile (F) with the pH of the 3-APP solution indicated inside the image.

D) Image of the phantom used for pH profile (G) with the pH of the two 3-APP solutions indicated for the NMR tubes immersed in saline.

E) Image of the phantom used for pH profile (H) with the pH of the three 3-APP solutions indicated in analogy to image (D). All phantom images were acquired with coronal slice orientation.

F - H) pH profiles of phantoms described in (C-E).

I) - L) pH profiles based on two NMR tubes filled with 3-APP solutions at different pH, and immersed in saline (phantom design as shown in D). The 3-APP concentration of the low-pH solution decreases from left to right. The vertical dashed lines indicate the borderlines between the low and high-pH regions within each pH profile, used for the integration of separate areas for the  $\text{pH}_{e1}$  and  $\text{pH}_{e2}$  regions.

Shaded areas in images indicate regions saturated by OVS during subsequently performed localized  $^{31}\text{P}$  NMR spectroscopy.

Figure 5. MRI cross sections for mouse tumor xenografts.

A) Glycolysis-deficient CCL39/ $\text{gly}^-$  tumor (see Fig. 3 B).

B) Glycolysis-deficient CCL39/ $\text{gly}^-$  tumor (see Fig. 3 A).

C) Wild-type CCL39 tumor (see Fig. 2 H).

D) Wild-type CCL39 tumor (see Fig. 3 C).

E) Wild-type CCL39 tumor (see Figs. 2 F, 3 D).

F) Wild-type CCL39 tumor (see Fig. 2 E).

G) Wild-type CCL39 tumor (see Figs. 1 A, 2 G).

The cross sections (1-mm slice thickness) cover the tumor volumes used for the measurements of pH heterogeneity by localized  $T_1$ -weighted  $^{31}\text{P}$  NMR spectroscopy. Shaded areas in images indicate regions saturated by OVS during subsequently performed localized  $^{31}\text{P}$  NMR spectroscopy. Dark-appearing tumor areas stem from (hemorrhagic) necrosis.

### **Quick Guide to Equations and Assumptions**

The current standard procedure for deriving a pH value from a pH-sensitive  $^{31}\text{P}$  NMR resonance is based on converting the chemical-shift axis of the resonance line into a pH axis (9). It is generally assumed that, after appropriate intensity correction, (i) the resulting curve adequately reflects the pH within the measured volume, and (ii) the position of the maximum of this pH curve represents "the" pH. We adopt assumption (i), within certain limits. However, we argue that the maximum of a tissue pH curve often yields a nonrepresentative pH value, because such curves are frequently asymmetric and irregularly shaped. We also contend that an (intracellular or extracellular) pH curve can and should be exploited to quantitatively analyze the respective underlying pH heterogeneity. For a detailed introduction into our algorithms see Section S1.

We propose to consider the (digitized) pH curve as an effective pH distribution curve, and to approximate it as a histogram where each digital curve point  $k$  corresponds to a histogram bin. From each curve/histogram we derive the following basic pH parameters:

$$\text{WEIGHTED MEAN pH:} \quad \overline{\text{pH}} = \frac{\sum_{k=1}^m (\text{pH}_k \times W_k)}{\sum_{k=1}^m W_k} \quad \text{eq. (1)}$$

where  $\text{pH}_k$  is the intracellular or extracellular pH value for a given digital point  $k$  of the pH curve;  $m$  is the total number of curve points used for calculation; and  $W_k$  is the scaled weight (ordinate value) of curve point  $k$ . Scaled weights are weights that have been adjusted to account for the variability of pH intervals between curve points. The non-equidistant character of pH curve points results from the non-linearity between the chemical-shift and pH scales. Thus, digital curve points that are equidistant on the chemical-shift axis are non-equidistant on the pH axis after point-by-point conversion. Weighted pH mean values directly derived from pH curves *without rescaling* would *overemphasize* pH regions represented by

relatively "dense" curve points. Scaled weights are also needed for the calculation of the other pH parameters presented below. However, pH modes (curve maxima) have to be obtained directly from the pH curve, because this curve is a representation of the distribution of pH values.

$$\text{WEIGHTED MEDIAN pH: } \quad \widetilde{\text{pH}} = \text{pH}_{\tilde{k}} + (\text{pH}_{\tilde{k}} - \text{pH}_{\tilde{k}-1}) \times f_{\text{int}} \quad \text{eq. (2)}$$

where  $\text{pH}_{\tilde{k}}$  is the pH value of curve point  $\tilde{k}$  possessing the cumulative sum  $\text{CSUM}(\tilde{k})$ ;  $\text{pH}_{\tilde{k}-1}$  is the pH value of curve point  $(\tilde{k} - 1)$  possessing the cumulative sum  $\text{CSUM}(\tilde{k} - 1)$ ; and  $f_{\text{int}}$  is an interpolation factor defined as  $f_{\text{int}} = \frac{(\frac{\text{CSUM}(m)}{2} - \text{CSUM}(\tilde{k}-1))}{\text{CSUM}(\tilde{k}) - \text{CSUM}(\tilde{k}-1)}$ . Cumulative sums are calculated for scaled weights of curve points. Conventionally, the median is the numerical value separating the higher half of a sample from the lower half, or the mean of the two middle values. For a series of weighted values, the location of the "weighted middle" has to be determined by interpolation. This is achieved by the interpolation factor  $f_{\text{int}}$  that determines the location of the weighted middle between two adjacent curve points,  $\tilde{k}$  and  $(\tilde{k} - 1)$ , corresponding to the cumulative sums (of scaled weights) that lie just above and below, respectively, the half-sum of the last point of the pH range used.  $\frac{\text{CSUM}(m)}{2}$  is defined as the half-sum of a series of  $m$  values.

SKEWNESS of pH distribution:

$$G1 = \frac{n}{(n-1)(n-2)} \sum_{k=1}^m W_k \left( \frac{\text{pH}_k - \overline{\text{pH}}}{s} \right)^3 \quad \text{eq. (3)}$$

where  $s = \sqrt{\frac{\sum_{k=1}^m W_k (\text{pH}_k - \bar{\text{pH}})^2}{(n-1)}}$  is the nominal standard deviation, a parameter analogous

to the standard deviation of the mean based on individual observations (= individual contributions to conventional histogram bins). In our algorithm,  $n = \sum_{k=1}^m W_k$  is a parameter analogous to the total number of individual observations in conventional histograms. Generally, both skewness and kurtosis (see below) characterize the shape of a statistical frequency distribution, i.e. asymmetry and pointedness, respectively. Hence, the absolute value of  $n$  is of no importance (as long as it is not too small) since these shape-related pH curve properties only depend on the relative weights of the individual pH curve values, and on their deviation from a normal distribution. We verified by computer simulation that skewness and kurtosis asymptotically approach  $n$ -independent values for  $n$  greater than several times the number of digital points  $m$ .

KURTOSIS of pH distribution:

$$G1 = \frac{n(n+1)}{(n-1)(n-2)(n-3)} \sum_{k=1}^m W_k \left( \frac{\text{pH}_k - \bar{\text{pH}}}{s} \right)^4 - \frac{3(n-1)^2}{(n-2)(n-3)} \quad \text{eq. (4)}$$

with parameters being defined as presented above for skewness.

ENTROPY of pH distribution:

$$H(W) = - \sum_{k=1}^m \left[ \frac{W_k}{\sum_{k=1}^m W_k} \log_2 \left( \frac{W_k}{\sum_{k=1}^m W_k} \right) \right] \quad \text{eq. (5)}$$

where  $H(W)$  is the entropy, and  $W$  is equivalent to the set  $P$  of all probability distributions as defined in the discrete Shannon entropy.

All algorithms used for calculating these five statistical parameters are based on established statistical equations; however, the original equations have been transformed for use in pH curve point analysis instead of conventional histogram analysis.

Table 1 Parameters characterizing  $\text{pH}_e$  heterogeneity, as obtained for well-defined test samples (A-D) and tumors (E-H), presented in Fig. 2 A-D and E-H, respectively.

	A	B	C	D
weighted average (mean), $\overline{\text{pH}_e}$	7.02	7.15	7.19	7.03
weighted median, $\widetilde{\text{pH}_e}$	7.02	7.32	7.30	6.99
mode, $\text{pH}_{e1}$	7.02	7.48	7.38	7.42
mode, $\text{pH}_{e2}$	-	6.59	6.56	6.64
mode, $\text{pH}_{e3}$	-	-	-	6.99
area ratios } $\text{pH}_{e2}$ vs. $\text{pH}_{e1}$	-	0.75	0.38	1.06
(integrated) } $\text{pH}_{e2}$ vs. $\text{pH}_{e3}$	-	-	-	0.69
area ratios } $\text{pH}_{e2}$ vs. $\text{pH}_{e1}$	-	0.72	0.37	1.05
(deconvolved) } $\text{pH}_{e2}$ vs. $\text{pH}_{e3}$	-	-	-	0.77
skewness, G1	0.15	0.01	-0.44	0.41
kurtosis, G2	0.13	-0.78	-0.22	0.33
entropy, H	3.95	4.81	5.00	5.09
	E	F	G	H
weighted average (mean), $\overline{\text{pH}_e}$	6.76	7.06	6.71	6.95
weighted median, $\widetilde{\text{pH}_e}$	6.79	7.03	6.61	6.89
mode, $\text{pH}_{e1}$	-	7.29	7.18	7.6 <sup>a</sup>
mode, $\text{pH}_{e2}$	6.83	6.72	6.48	6.72
mode, $\text{pH}_{e3}$	-	-	-	7.20
area ratios } $\text{pH}_{e2}$ vs. $\text{pH}_{e1}$	-	0.97	1.85	7.42
(integrated) } $\text{pH}_{e2}$ vs. $\text{pH}_{e3}$	-	-	-	2.18
area ratios } $\text{pH}_{e2}$ vs. $\text{pH}_{e1}$	-	0.99	1.98	4.02 <sup>a</sup>
(deconvolved) } $\text{pH}_{e2}$ vs. $\text{pH}_{e3}$	-	-	-	1.25 <sup>a</sup>
skewness, G1	-0.57	0.39	0.34	0.58
kurtosis, G2	0.49	-0.19	-0.38	-0.38
entropy, H	5.86	5.05	6.14	4.66

<sup>a</sup>: estimated values; five modes were needed for reasonable fit; fitted areas were combined for comparison with integrated areas.

Table 2 Parameters characterizing  $\text{pH}_i$  heterogeneity in tumors.

	A	B	C	D
weighted average (mean), $\overline{\text{pH}_i}$	7.15	7.18	6.99	6.77
weighted median, $\widetilde{\text{pH}_i}$	7.17	7.12	6.97	6.64
mode, $\text{pH}_{i1}$	7.23	7.03	7.20 <sup>a</sup>	-
mode, $\text{pH}_{i2}$	6.86	-	6.81 <sup>a</sup>	6.47
area ratios $\text{pH}_{i2}$ vs. $\text{pH}_{i1}$ (integrated)	0.74	-	1.39	1.88
area ratios $\text{pH}_{i2}$ vs. $\text{pH}_{i1}$ (deconvolved)	0.90	-	1.00	-
skewness, G1	0.07	0.99	0.28	0.64
kurtosis, G2	-1.16	1.21	-0.66	-0.06
entropy, H	5.78	1.19	6.63	1.71

<sup>a</sup>: estimated values. Data (A-D) are based on <sup>31</sup>P NMR signals of  $\text{P}_i$  obtained from tumors presented in Fig. 3 A-D.



Figure 2

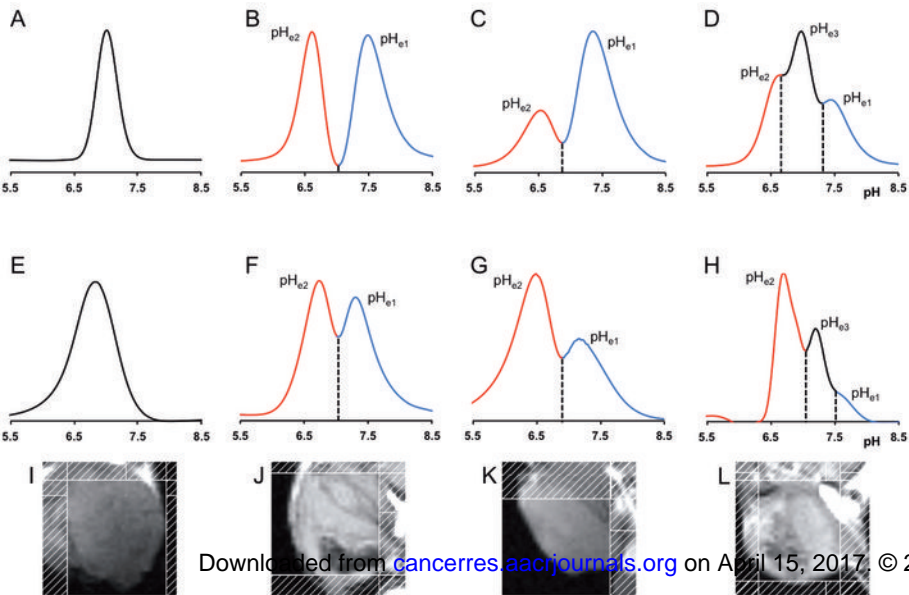


Figure 3

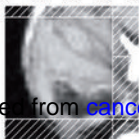
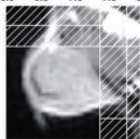
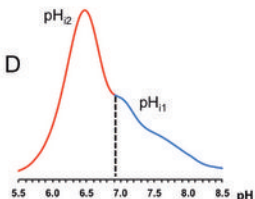
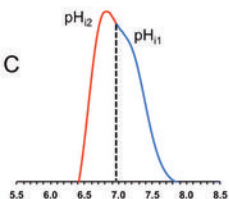
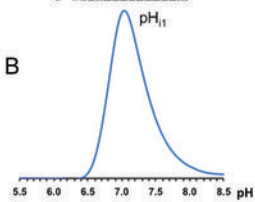
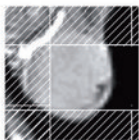
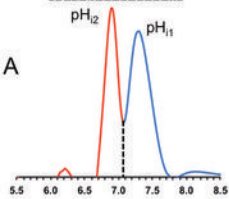
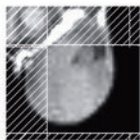


Figure 4

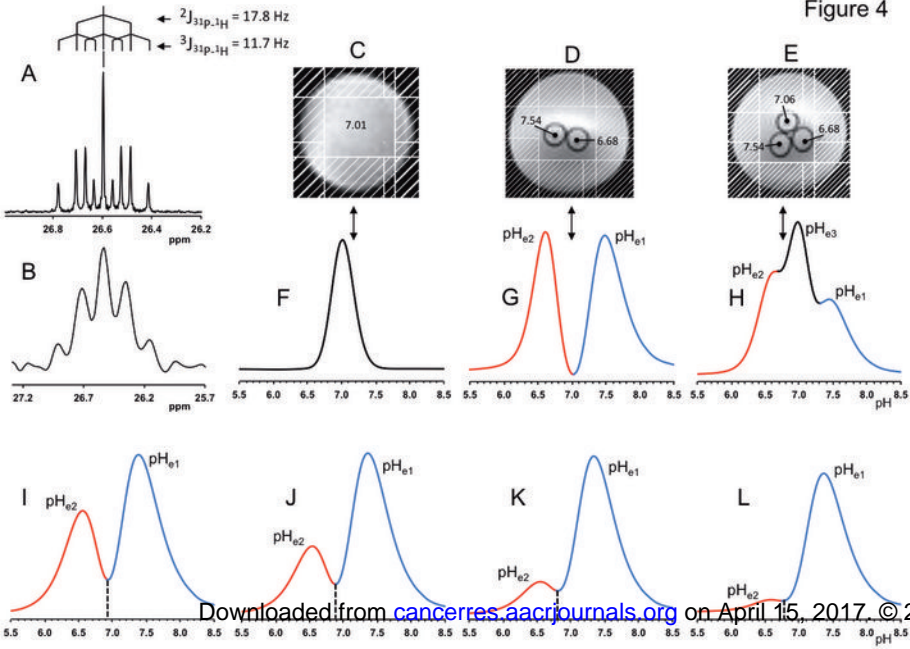
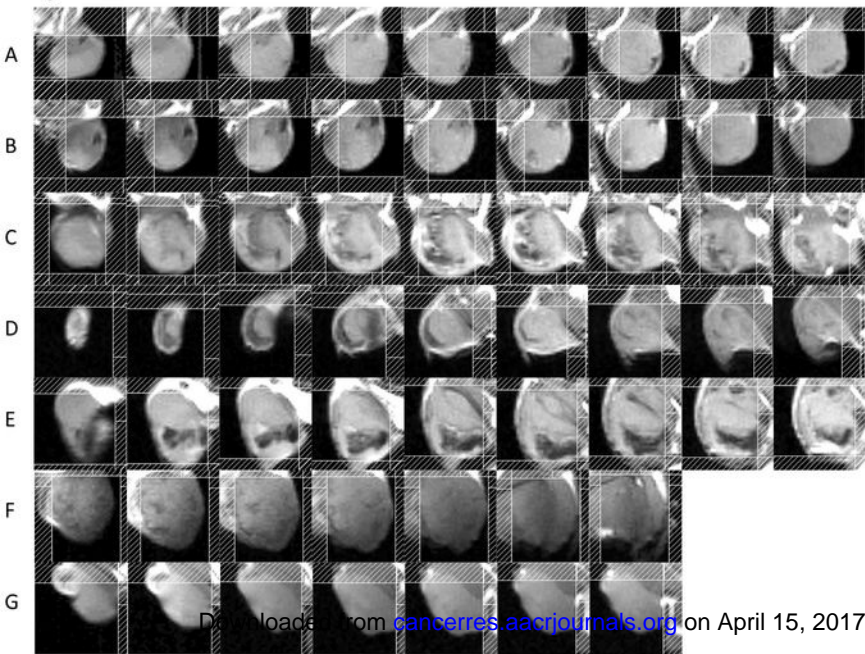


Figure 5



# Cancer Research

The Journal of Cancer Research (1916–1930) | The American Journal of Cancer (1931–1940)

## Quantitative in-vivo characterization of intracellular and extracellular pH profiles in heterogeneous tumors: a novel method enabling multiparametric pH analysis

Norbert W Lutz, Yann Le Fur, Johanna Chiche, et al.

*Cancer Res* Published OnlineFirst June 10, 2013.

<b>Updated version</b>	Access the most recent version of this article at: doi: <a href="https://doi.org/10.1158/0008-5472.CAN-13-0767">10.1158/0008-5472.CAN-13-0767</a>
<b>Supplementary Material</b>	Access the most recent supplemental material at: <a href="http://cancerres.aacrjournals.org/content/suppl/2013/06/10/0008-5472.CAN-13-0767.DC1">http://cancerres.aacrjournals.org/content/suppl/2013/06/10/0008-5472.CAN-13-0767.DC1</a>
<b>Author Manuscript</b>	Author manuscripts have been peer reviewed and accepted for publication but have not yet been edited.

<b>E-mail alerts</b>	<a href="#">Sign up to receive free email-alerts</a> related to this article or journal.
<b>Reprints and Subscriptions</b>	To order reprints of this article or to subscribe to the journal, contact the AACR Publications Department at <a href="mailto:pubs@aacr.org">pubs@aacr.org</a> .
<b>Permissions</b>	To request permission to re-use all or part of this article, contact the AACR Publications Department at <a href="mailto:permissions@aacr.org">permissions@aacr.org</a> .